Analysis of Structural and optical Interactions of the Precision optical Interferometer In Space (POINTS)

James W. Melody and Hugh C. Briggs
Jet Propulsion Laboratory "
California Institute of Technology
Pasadena, CA

Abstract

The Precision Optical Interferometer in Space (POINTS) is a free flying, space-hascd, astrometric interferometry mission employing an instrument with two 2-meter baseline interferometers whose baselines form an angle of 90°± 3°. POINTS will measure the angular distance between two stars roughly 90° apart to a precision of 5 microarcseconds (μas). POINTS is currently under joint study at California Institute of Technology's Jet Propulsion 1 Amatory (JP1.) and the Smithsonian Astrophysical Observatory (SAO). The interferometers use a fringe tracking, extended Kalman Filter in order to estimate the relative angle between the interferometer optical axis and the line connecting the spacecraft and the star. In order for this extended Kalman filter to track the fringes, the fringe coherence of each interferometer must be at least 95% (corresponding to changes in optical path difference of roughly ten nanometers) during the filter update period, given the propagation of disturbances through the spacecraft structure to the optical support structure. POINTS uscs a full aperture laser metrology system (FAM) to measure any changes in the starlight optical path difference (OPD) internal to each interferometer, and this measurement is used to actively correct for the changes in optical path difference.

This paper addresses a disturbance analysis of the preliminary POINTS spacecraft and instrument design in order to determine whether and to what extent any isolation and/or added structural damping is necessary to meet the POINTS instrument requirements. The analysis was performed using the Integrated Modeling of Optical Systems (1 MOS) integrated modeling tool. 1 MOS is an integrated software environment wherein structural, optical, and control system modeling can be performed, Linearized optical models, structural finite element models, and disturbance characterization models were developed and integrated in IMOS. Starlight fringe coherence was used as a metric to quantify the performance of the POINTS instrument. Linear optical perturbation analysis gave insight into the sensitivity of the performance of the interferometers to perturbations of the positions and orientations of the optical elements. Finite element modal analysis yielded structural modes, modeshapes, modal costs, and Hankel singular values. These models were integrated with the disturbance models allowing for generation of frequency response functions. The result of this analysis is end-to-end disturbance characterizations (starlight fringe coherence as a function of reaction wheel speed, for example).

2. POINTS Spacecraft Description

The baseline spacecraft configuration for POINTS is shown in Fig. 1 [1]. POINTS consists of a spacecraft bus, the astrometric instrument, and a two-axis gimbal. The gimbal separates the instrument and the spacecraft bus. The bus holds the majority of the spacecraft hardware, (reaction wheels, command and data handling electronics, batteries, etc.), whereas the instrument (contained in the large hatbox enclosure) contains the starlight interferometers, the metrology interferometers, and other associated hardware. The spacecraft bus is used to shield the instrument from the sun, in order to provide a more stable thermal environment for the instrument. The two-axis gimbal is required in order to enable the instrument to view star pairs across the entire sky (except for those near the sun) [2]. In order to allow for a larger set of target star pairs, the angle between the interferometers must be articulated. **The range of articulation** will be roughly ± 3°. POINTS will measure the angular separation of two stars by viewing thcm with the starlight interferometers for several minutes. In the baseline configuration, the instrument is pointed in three rotational degrees of freedom (dof) by the inner (spin-axis) gimbal axis, the outer (tip-axis) gimbal axis, and by rolling the spacecraft about the direction to the Sun (see Fig. 1).

2.1 Structural Design

The optical bench is the structure inside the. instrument enclosure that supports the optical elements, lasers, detectors, and metrology hardware. The baseline optical bench design is an aluminum metering truss structure with a cross section of 50cm square. The truss is constructed of thin walled tubes with a cross section of onc inch (2,54 cm) and a wall thickness of 50mils (1 .27mm). The two instrument metering trusses (one for each starlight interferometer) arc both mounted on a tubular central column structure, This central column has a diameter of 50cm and a wall thickness of one inch (2.54 cm) [3].

The spacecraft bus structure uses a thin (50mil/1.27mm), riveted aluminum skin with stiffeners. The gimbal yoke is assumed to have a similar construction (thin aluminum skin with stiffeners) [31. The instrument enclosure is needed primarily to provide benign thermal and contamination environments. The instrument enclosure

will either be a stiff honeycomb sandwich construction covered with multi-lay yer insulation (M I. I), or an open framework of bar elements supporting MI.I. The enclosure design is as yet undecided.

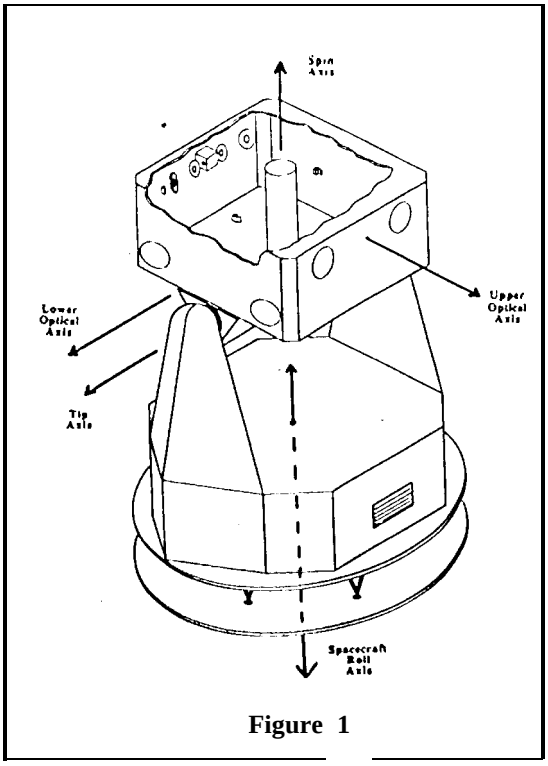

Figure 1

2.2 Slew mechanisms

In order to slew the instrument between star pairs, the attitude and articulation control system (AACS) uscs reaction wheels, located in the spacecraft bus, to supply torque to the space.craf[. Electromagnetic motors (either stepper motors or dc brushless motors) arc used to actuate the instrument in the gimbal. An articulation mechanism (AM) is used to change the angle between the interferometers. The AM will be a stepper motor driven lead screw actuator connecting the top and bottom interferometer optical support structures. During target star observations, both the gimbal and the articulation mechanism will be locked in place.

2.3 Target star measurement

During target star observations, the POINTS instrument measures the angle between the two stars by measuring the angle between the interferometer optical axis (normal to the interferometer baseline) and the line joining the spacecraft and each star (the star line) for each interferometer and by measuring the angle between the interferometer optical axes. This measurement scheme is shown in Fig.2. Each starlight interferometer measures the angle between its optical axis and its target star line (its star angle, δ). A set of laser gauges, known as the angle metrology system, measures the angle between the interferometer optical axes (φ).

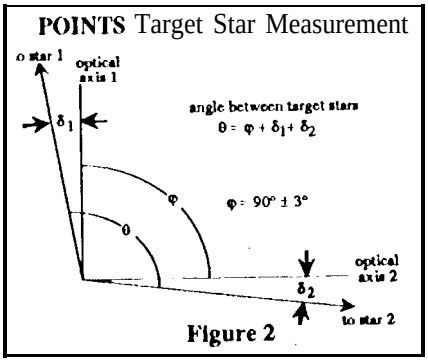

Figure 2

2.4 Star angle measurement

The starlight interferometers measure the star angles by actually measuring the difference between the optical paths from the star to the interferometer detector, known as the optical path difference (OPD). For a small star angle, the optical path difference is the star angle times the baseline (Fig.3). A star angle measurement accuracy of 5 pas for a 2-meter baseline interferometer corresponds to an OPD measurement accuracy of 48 picometers (pm). On this scale, the OPD measured by the interferometers will include optical path differences duc to misalignments and misplacements of the optical elements (internal optical path differences). The starlight interferometers cannot differentiate between internal OPD and OPD duc to the star angle. The OPD measured by the instrument will be called total OPD to differentiate it from internal OPD and star angle OPD.

The full aperture metrology system will sense the changes in internal OPD. The measured internal OPD will then be used as feedback to minimize the internal OPD by translating the beamsplitter accordingly. This internal OPD control system will be a low bandwidth control system in order to avoid any interactions between the control system and the dynamics of the optical metering truss structure. Thus, the internal OPD control system will be a quasi-static control system correcting for assembly misalignments and thermal deformations. It will not correct for any structural vibration induced internal OPD,

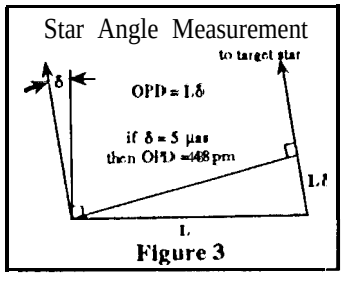

Figure 3

A schematic of the optical prescription of a single starlight interferometer is shown in Fig.4 [4]. The starlight interferometers usc a channeled spectrum to measure OPD. This channeled spectrum detection involves sending the interfered collimated beam through a prism and/or grating before focusing the starlight on the detector arrays (Fig.5). The usc of channeled spectra relaxes the requirements on the pointing accuracy of the instrument, but has no effect on the OPD stability requirement. A single starlight interferometer uscs an array of 128 detectors to detect

the. intensity of the starlight interference fringes.

The fringe intensity across the detector array is shown in Fig.6, assuming a linear dispersion and a small dispersion angle. The spatial period of the intensity pattern at the detector is inversely proportional to the OPD. Thus, as the total OPD gets larger, or similarly as the star angle gets larger, the spatial frequency of the intensity pattern at the detector gets larger, and more fringes appear on the detector.

The separate detectors measure this intensity over their finite width (Fig.6). Since the spatial dimension is proportional to the optical frequency of the refracted light (under the assumptions mentioned above), this corresponds to integrating over a small portion of the optical bandwidth.

The output of the detector array of an interferometer is a set of measured intensities. From this set of measured intensities, the star angles arc estimated with the usc of an extended Kalman filter (the fringe tracking filter). It is estimated that the detector integration times (hence the filter update rate) will bc at most 0.2 seconds. This period is required for the starlight interferometers to obtain enough photons so that the photon signal-to-noise ratio is greater than five (assuming 2m baselines, 25cm apertures, an overall photon detection efficiency of 20%, and a target star of apparent visual magnitude 15).

POINTS optical Prescription

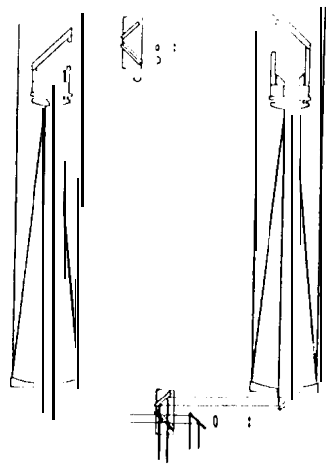

Figure 4

2.5 Tots] OPD accuracy and stability requirements

Since the internal OPD control system corrects for any quasi-static internal OPD, total OPD accuracy is actually star angle OPD accuracy, hence interferometer pointing accuracy. The pointing accuracy requirement derives from the requirement that each detector span only a fraction of a spatial fringe.

POINTS Channeled Spectra

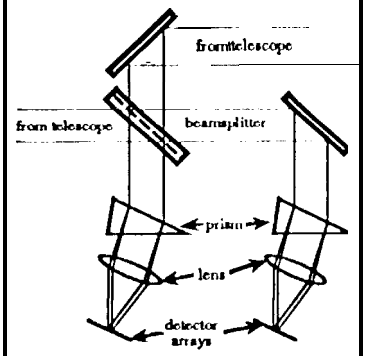

Figure 5

The total OPD stability requirement is determined by the robustness of the fringe tracking filter in the presence of fringe jitter. Fringe coherence, defined in Eq. 1, is a measure of fringe stability. Until detailed analysis of the fringe tracking filter is performed, it is assumed that the filter can track fringes if the fringe coherence, at all detector optical frequencies, is above 95% (corresponding to a change in OPD of 12.7 nanometers for the lowest instrument wavelength, 0.25μm). As defined in Eq. 1, fringe coherence is inversely related to the square of optical wavelength. (The POINTS instrument will measure optical wavelengths from 0.25μm to 0.9μm.) This agrees with intuition that would lead us to believe that a given change in OPD is less significant for a larger wavelength.

$$C \equiv \exp\left[-2\left(\frac{\pi}{\lambda}\sigma_{OPD}\right)^2\right] \qquad (1)$$

where, C is the fringe coherence

λ is the optical wavelength

σ_{OPD} is [hc rms total OPD variation during the detector integration time

It is significant to note that σ_{OPD} is the rms of the total OPD variation *during the detector integration time* (a.k.a., bin time). The "smear" of the measured fringe intensity during the detector bin time is the quantity significant to the quality of a single intensity measurement, much as the smear of an image is to the quality of an image. The rms of the difference of the instantaneous OPD and the moving average OPD during the bin time is the appropriate OPD stability metric. This metric was developed by San Martin and Sirlin in [5] and is defined in Eq.2. The essence of the frequency weighting function defined in Eq.2a is this: for a given exposure or integration time, a low frequency (compared to the exposure frequency) disturbance of a given amplitude is lcss detrimental than a high frequency disturbance of the same

Intensity at Detector Array, $I_d(x)$

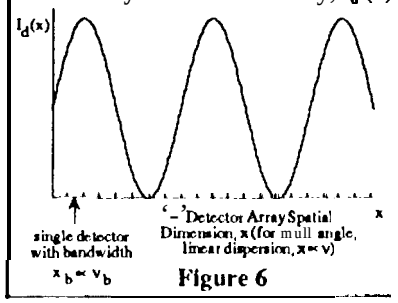

Figure 6

amplitude. Thus disturbance frequencies below the exposure frequency are weighted less.

$$(\sigma_{OPD})^2 \equiv 2\pi \int_{-\infty}^{\infty} S_{OPD}(\omega) W_s(\omega T) d\omega \qquad (2)$$

where, $S_{OPD}(\omega)$ is the power spectral density of the total OPD
T is the integration time
ω is frequency (in rad/s)
$W_s(\omega T)$ is a weighting function defined by

$$W_s(y) \equiv 1 - 2\left[\frac{1 - \cos(y)}{y^2}\right] \qquad (2a)$$

3. POINTS Integrated System Model (ISM)

3.1 POINTS integrated system modeling motivation

Because of the complex, nanometer-level interactions between the optical metering truss structural dynamics and the distributed optical elements, it was decided that an integrated system model was needed to perform an end-to-end mechanical disturbance analysis. Specifically, a model whose input is mechanical disturbances and whose output is fringe coherence is required. 'I'his end-to-end disturbance analysis should include a detailed spacecraft finite element model, a disturbance model, and a detailed optical model. Since POINTS is still in a relatively immature phase of design, these models were not available in tbc detail that is preferred in order to perform an end-to-end disturbance analysis. To some extent, this immaturity in the design of POINTS was duc to a lack of understanding of the relationships between the performance of the subsystems. An effort was made to generate models that would roughly characterize the expected performance of the spacecraft, given the present state of maturity of the design. It was hoped that the results of this initial integrated system analysis would yield insight into the complex subsystem interactions and thus bc used to influence the separate subsystem designs. When more mature designs arc formulated, the integrated model will bc updated to reflect these design improvements.

IMOS, though still in development, provides a very useful environment for this type of analysis. IMOS brings together finite element modeling capabilities, control system design tools, linear system analysis tools, optical ray trace capabilities, and, by interfacing with tbc Controlled Optics Modeling Program (COMP), optical linear perturbation analysis in a single, interactive environment (presently Pro-MATLAB from The Math Works, Inc. [6]). This uniform analysis and modeling environment is essential to gaining understanding of the subsystem interactions by performing system level trade studies. This environment also allows for easy incrementation of the subsystem module level of detail.

The specific goals of this analysis were 1) to predict starlight interferometer performance in the presence of mechanical disturbances, and 2) to identify design options that may meet the interferometer performance goals and estimate their relative effectiveness.

3.2 POINTS integrated system model scope

As mentioned above, in order to perform a characteristic, end-to-end mechanical disturbance analysis, a mechanical disturbance model, a structural finite element model, and a linear optical model must bc developed. Since tbcy arc not necessary for a mechanical disturbance. analysis, neither a thermal model nor an AACS model is used. Tbc structural design options assessed in terms of improving instrument performance in the presence of mechanical disturbances arc passive isolation of the disturbance sources, and the usc of passive/aclivc damping struts in the structure.

Although certain portions of the POINTS structural design were mature enough to generate detailed finite element models, the POINTS study team dccidcd not to model these components in detail. These detailed component models would have resulted in large (=1000 degrees of freedom) finite element models. This is undesirable for two reasons: 1) The computation time required for this large finite element problem would have been long enough that the analysis process would have no longer been interactive (solution times up to roughly 30 minutes). 2) IMOS, in its present state, cannot solve finite element problems above roughly 400 degrees of freedom accurately. Along with these reasons, it was believed that the extra degrees of freedom would not significantly change the resultant lower frequency modes (<1000Hz), which arc the modes of interest.

Instead of a detailed modeling approach, mode] fidelity was judiciously added to the areas of most significance (the instrument metering truss and, to a lesser extent, the gimbal structure). The structural model includes the spacecraft metering truss, the gimbal structure, and the spacecraft bus, with decreasing model fidelity in

that order. The instrument enclosure is not modeled, due to the required modeling complexity. Since the instrument housing dynamics are expected to have a significant effect on the instrument performance, this is a short-coming of the structural finite element model. Because the solar panel is rigidly fixed to the spacecraft bus (hence away from the instrument), the solar panel dynamics are not modeled.

The optical mode] ing includes modeling of the upper and lower starlight interferometers. Since the optical elements after the beamsplitter have no bearing on the internal OPD, these focal plane optics were not modeled. A model of the FAM was not included since the internal OPD control system is a quasi-static control system, and has no effect on motion at structural modal frequencies. Since the articulation mechanism is assume.d to be locked during observation, the angle metrology system performance has no effect on the performance of the starlight interferometers. As such, the angle metrology system was not modeled.

Reaction wheel assembly (RWA) mechanical disturbances are the only mechanical disturbances that affect instrument performance. POINTS will usc solid state recorders, so there will be no tape recorder disturbances, Although the internal OPD control system actuator will have some reaction force, the quasi-static control system will produce very small disturbances (forces required for nanometers of motion) at frequencies much lower than structural dynamics frequencies. Since it is not clear if POINTS will carry a cold gas propulsion system for momentum management, the effects of liquid fuel sloshing were not modeled. I'bus, only RWA mechanical disturbances are modeled,

3.3 POINTS integrated system modeling process

When performing an integrated model analysis, the modeling and analysis process is as important as the results. It is during the modeling process, as well as when examining analysis results, that intuition is gained into the subsystem interactions. A block diagram of the POINTS integrated modeling process is given in Fig.7. The process begins with the development of both a structural finite element mode] and the starlight interferometer optical models. The finite clement model consists of a nodal geometry, element connectivity, element properties, and nodal boundary conditions (whether the nodes arc fixed, constrained, or free). The optical models arc comprised of optical element locations, orientations, and shapes From the finite element model, structural modal analysis is performed, yielding both rigid-body and flexible-body modes and modeshapes. The starlight optical models arc used to generate linear optical perturbation models. These models give change in optical parameters (e.g., optical path length) as a linear function of change in the positions and orientations of the optical elements. By combining the linear optical perturbation model and the finite element modal analysis, the sensitivity of starlight OPD to each modeshape (modal cost) is calculated.

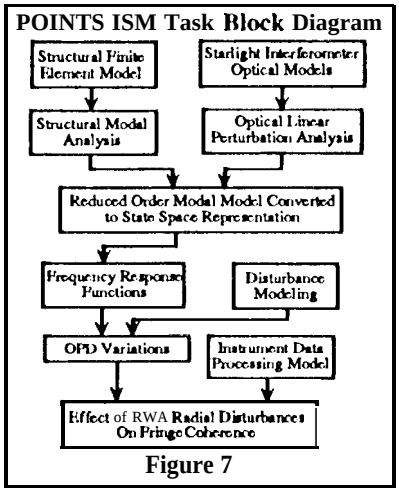

Figure 7

Next, the optical and structural models arc combined into a single first-order state-.cwacc model. This involves reducing the order of the modal model by eliminating the flexible-body modes that arc less significant to the desired input-output relationships: reaction wheel disturbances to OPD variations. Hankel singular values arc used to evaluate the significance of the flexible-body modes to the input-output relationships. All rigid-body modes arc included in the model. A low level of uniform modal damping is assumed for the flexible-body modes, The modal model is then transformed into first-order state-space form, and the optical perturbation model is included in the measurement equation, At this point, there exists a firs(-order state-space model whose input arc disturbance forces and torques at chosen structural nodes, and whose output arc total OPD variations of the two starlight interferometers. From this linear system model, frequency response functions can be generated.

These frequency response functions can be combined with reaction wheel disturbance force models to yield the effects of these disturbances on starlight OPD. From these OPD variations, fringe coherence can be calculated, yielding the effects of reaction wheel disturbances on fringe coherence.

In order to study the effectiveness of passive isolation, the input disturbances arc filtered by the isolation system before being input to the state space model. The passive/active damping option is studied by increasing the modal damping of the targeted structural modes assumed in the generation of the state space model, In both cases, the effects of disturbance.s on starlight fringe coherence arc calculated. These arc then compared to the hard-mounted, undamped-structure results.

4. Structural Finite Element Model (FEM) and Modal Analysis

4.1 POINTS structural FEM description

The POINTS finite element model is depicted in Fig.8. The model consists of the instrument metering truss, the gimbal structure, and the spacecraft bus. Neither the housing structure, nor the housing mass arc modeled. Beam elements (modeling axial, bending, and twisting stiffness) are. used throughout the model, and the translational as well as rotational motion of the. nodes arc modeled, resulting in 360 degrees of freedom. The instrument was modeled in the gimbal position shown in Fig.8. Although the structural dynamics will vary significantly with gimbal position, it is assumed that this model will roughly characterize the spacecraft dynamics, irrespective of gimbal position.

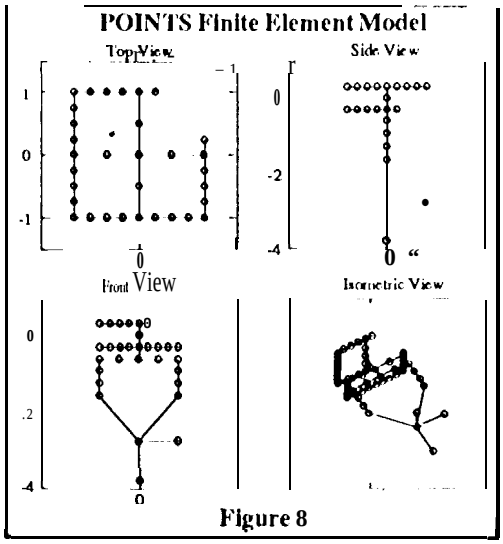

Figure 8

Instead of modeling each truss rncmbcr of the optical bench as a single FEM structural element ("stick-by-stick model"), the square cross-section metering truss was modeled as a line of beams. This was done in order to reduce the number of degrees of freedom. Equivalent beam masses and stiffnesses were generated from the expected geometry and n~ass/stiffness properties of the metering truss elements [3]. This line-of-beams model of the metering truss was populated with sufficient FEM nodes so that some "local" modes of the optical bench itself arc captured. The AM bearings and the AM itself arc assumed to be infinitely stiff. An effort was made to place finite element nodes at or near the locations of optical elements, in order to ease the integration of the structural and optical models. The appropriate mass of the optical elements was added to the r odel.

The gimbal structure was also modeled with lines of beams. Again, the model was sufficiently populated with nodes to enable the modeling of gimbal structure "local" modes. The equivalent beam properties were found by considering the gimbal structure geometry and n~ass/stiffness properties [3]. Since the gimbal actuators will bc locked during observation, and since the gimbal bearings arc fair] y stiff (≈ 107 N/m) [3], the gimbal bearings and the gimbal motors arc assumed to bc locked.

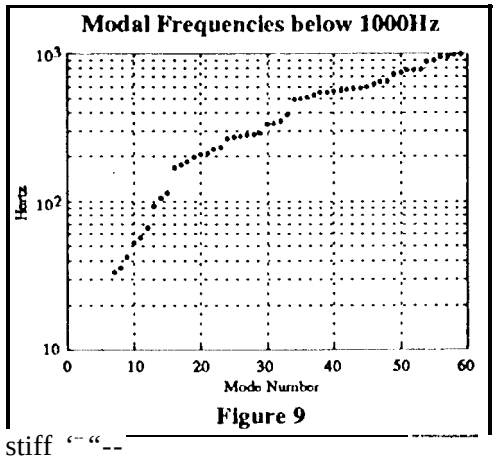

Figure 9

The spacecraft bus is modeled by four rigidly attached nodes, which form three mutually perpendicular line segments. The center node represents the center of mass of the spacecraft bus and contains most of its mass, while the other three nodes represent the locations of the three reaction wheels. These three nodes were used to provide a moment arm for the reaction wheel forces. In the present model, no spacecraft bus modes arc modeled. Since IMOS currently cannot incorporate. constraint equations, the elements attaching the four nodes arc c-onncctcd to each 'other and to the gimbal yoke by very stiff (effectively rigid) beam elements.

4.2 FEM Modal Analysis Results

After the finite element model was formulated, the finite element eigenproblem was solved, yielding structural modes and modeshapes. The solution included both rigid-body and flexible-body modes, and both sets of modes were used in the end-to-end disturbance analysis. (For more information on solving finite element eigenproblems in IMOS see [7].) This means that the results represent both flexible-body dynamics effects and open loop pointing jitter effects. The modal frequencies of the flexible-body structural modes below 1000Hz (modes 7 through 57) arc shown in Fig.9. The lowest flexible-body modal frequency was found to bc 34.6} Iz.

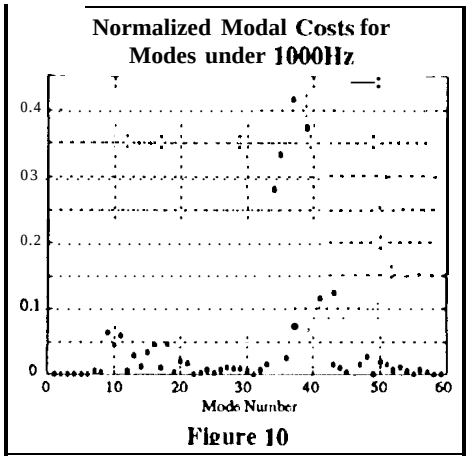

Figure 10

The modal cost for the flexible-body modes below 1000Hz is shown in Fig. 10. This modal cost is a measure of the relative sensitivity of the starlight internal OPD to a given mass normalized modeshape. A

higher modal cost signifies more. sensitivity of internal OPD to the given mode. It is clear from Fig. 10 that, of the lower frequency modes, mode 9 significantly affects instrument performance. The modeshape of mode 9 is shown in Fig. 11.

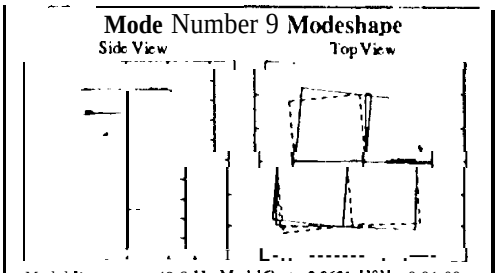

Figure 11

It was determined that two structural motions were found to be critical to instrument performance: interferometer spin motion and in-plane warping of the interferometers causing oul.of-phase pistoning of the siderostat mirrors. The spin motion, in particular, participates in the modeshape of several modes with relatively low frequencies (as low as 43.3} 17,). It was deduced that three structural design characteristics affect the modal frequencies related to these critical motions: 1) the stiffness of the central column, '2) the offset of each interferometer center of mass from the central column axis, and 3) the offset of the instrument center of mass from the gimbal tilt axis. It is desirable to increase the modal frequencies related to these motions since this makes the motions icss significant in the end-to-end disturbance analysis. By increasing the stiffness of the central column, the modal frequencies related to interferometer spin will increase. On the other hand, by eliminating the two center of mass offsets, the reduced modal mass participation of the cantilevered components will increase the modal frequencies of all modes discussed. Unfortunately, rotating the instrument about its center of mass in the gimbal tip axis may not allow enough sky coverage. However, stiffening the central column and attaching each interferometer to the central column with its center of mass on the spin axis should be considered.

S. Starlight Interferometer optical Models and Analysis

The optical modeling and analysis process consists of generating nominal optical prescriptions, performing linear differential ray traces to create linear optical models, and manipulating the linear optical models in order to facilitate the system model integration. Generation of the optical prescription and manipulation of the linear optical models arc performed in the 1 MOS environment (Pro-Matlab). The linear differential ray trace is performed in COMP. I MOS includes translation functions to facilitate this interaction,

5.1 Optical prescription generation

In IMOS and COMP, an optical prescription consists of locations, orientations, and shapes of optical elements in some global coordinate system [8]. Although there was no detailed optical design when the integrated modeling was performed, sufficient information was available to generate optical prescriptions of the starlight interferometers. The starlight interferometers usc two siderostat mirrors whose centers arc 2m apart (for a 2m baseline). These siderostat mirrors direct the starlight into two afocal Cassegrain telescopes (parabolic primary and secondary) with a 10:1 beam compression ratio, an aperture of 25cm, and a primary mirror focal length of 1 m. The output of these telescopes is then joined at the beamsplitter. This optical configuration is known as the FAM-A configuration. Aside from this given information, assumptions were made about the dimensions of the beamsplitter and the location of the primary mirrors relative to the beamsplitters.

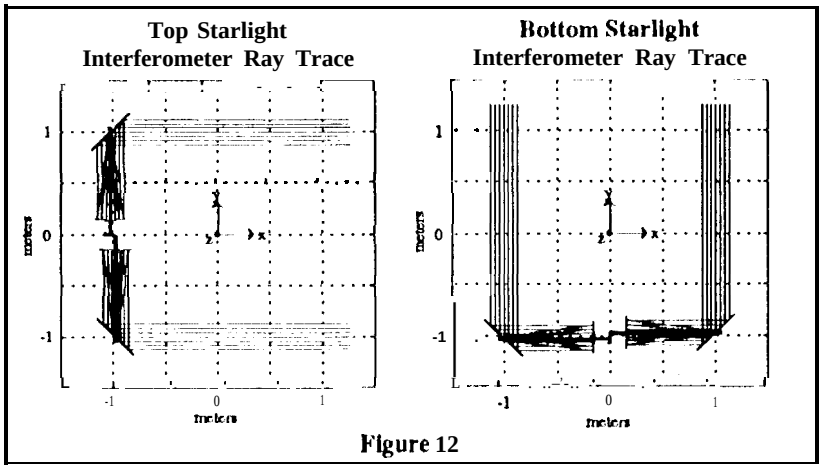

Figure 12

In order to model both starlight interferometers, eight optical models arc required: onc for each interferometer arm to each detector (i.e. for each interferometer, each combination of an arm and a detector). It is assumed that the OPD variations at each detector of a single interferometer will be the same, thus only onc detector per interferometer is modeled, This results in four optical models. As mentioned above, focal plane optics arc not modeled. Therefore, the detectors arc placed directly after the beamsplitter.

These optical prescriptions were generated in IMOS with the help of its interactive ray trace capability. This capability allows for incremental generation and debugging of the optical prescriptions (i.e., optical elements can be added and checked onc at a time down the optical train). Generating the optical prescriptions in IMOS also

allows for parameterization of the optical models. The starlight optical models were parameterized in terms of beamsplitter dimension and the distance between the primary mirror and the. beamsplitter, so that these quantities could be easily changed when specified by a detailed optical design. The optical prescriptions were specified in terms of the structural model global coordinates. The ray traces of the. top and bottom interferometers are shown in IJig.12. These optical prescriptions were then translated to COMP input files in order to perform linear differential ray traces.

5.2 COMP linear differential ray trace analysis

The next step in the optical modeling process is to perform linear di fferential ray traces in COMP in order to calculate linear optical perturbation models. These linear models are of the form:

$$\vec{dy} = C_{opt}\vec{dx} \qquad (3)$$

where, $\vec{dy}$ is a vector of changes in optical path length for each ray
C_{opt} is a matrix of analytic partial derivatives
$\vec{dx}$ is a vector of optical element position and orientation perturbations

By performing differential ray trace analysis on the four optical models mentioned above, four linear optical models (C-matrices) are generated which relate position and orientation perturbations of the starlight interferometer elements to change in OPL (ΔOPL) of each ray. Each C-matrix has dimension (# of rays) -by-(# of optical elements)*(6 degrees of freedom). These C-matrices are. then written into .m-files that are loaded into the IMOS environment. [6] [8]

5.3 Linear optical model manipulation

At this point, the C-matrices represent AOP1, of a single interferometer arm for each ray as a function of the motions of each optical element. We would like C-matrices to yield a single OPD variation for each starlight interferometer as a function of structural node motion, in order to simplify the integration of the structural and optical models. Thus, manipulation of the C-matrices is required.

First, it is necessary to condcnsc the partials of all rays for a given input perturbation and output optical parameter into a single number. At present, partials are given with respect to a planar reference surface, perpendicular to the nominal direction of propagation of the wavefront. In reality, this wavefront will be focused by some focal plane optics onto the actual detector. Thus, to the extent that the focal plane optics are well designed, the ΔOPL at the flat reference surface for each ray will be the same as the ΔOPL for each ray at the actual detector. Thus, the AOP1, measured at the actual detector for a given interferometer arm is the average of the AOPL output of the linear model. This is done by averaging the C-matrix elements for each structural degree of freedom.

Next, the C-matrices for each arm of an interferometer are subtracted so that the two resultant C-matrices give OPD variation for each starlight interferometer as a function of structural node motion. Thus, given any structural perturbation vector, top and bottom interferometer OPD variation can be calculated. The optical modal costs discussed above were generated in this manner: each mass normalized modeshape was multiplied by the two C-matrices, and the absolute value of the two resultant OPD were summed to yield a single modal cost value,

By examining the C-matrices it was determined that the starlight interferometers are more sensitive to translational motion of the optical element structural nodes than they are to individual rotations of these nodes (by at least a factor of 15). This is not to say, however, that the interferometers are insensitive to z-axis rotation of the entire interferometer. On the contrary, the interferometers are sensitive to this rotation, but this is primarily duc to the translations of the individual elements associated with this rotation rather than the z-axis rotation of the individual elements.

6. Reaction Wheel Mechanical Disturbance Models

As mentioned above, the only mechanical disturbances expected on POINTS are reaction wheel disturbances. Reaction wheel mechanical disturbances are classified into four categories: axial torque disturbances, radial torque disturbances, and axial and radial force disturbances. Empirical disturbance models developed for the Hubble Space Telescope (11ST) reaction wheels were used [9]. These models were assumed to yield mechanical disturbances that are characteristic of the POINTS reaction wheel disturbances.

Radial forces are forces normal to the spin axis of the reaction wheel (in two axes), and axial forces are forces along the spin axis of the reaction wheel. All of these disturbances exist at discrete frequencies which are (non-integer) multiples of the wheel speed. Similarly, radial torque disturbance components exist at multiples of wheel speed, Axial torque disturbances are torque disturbances that are manifested as variations of the RWA commanded torque. Axial torques were determined to be insignificant, and are not included in the end-to-end model.

For radial torques, axial forces, and radial fore.cs, the amplitudes of the disturbance components arc functions of the square of the wheel speed, In each case, the force disturbances arc modeled by Eq.4 [9],

$$hi(t) = \sum_{i=1}^{n} C_i (\omega_{rw})^2 * \sin(h_i \omega_{rw} t + \psi) . \quad (4)$$

where, **hi** is the. disturbance harmonic
C1 is the disturbance harmonic's coefficient
ωrw is the reaction wheel speed in rad/s
M is the. modeled moment (torque or force)
ψ is some random phase

7. integration of Optical and Structural Models

The next step in the integrated modeling process is to integrate the optical and structural models into a single first-order stale-space linear system. This is done in order to take. advantage of the analysis capabilities in the Pro-MATLAB environment [6].

7.1 Conversion to first-order linear system model

The general first-order sfatc-spat.c description is given in Eq.5.

$$\dot{\vec{x}} = A\vec{x} + B\vec{u} \quad \text{(stale equation)}$$
$$\vec{y} = C\vec{x} + D\vec{u} \quad \text{(measurement equation)} \quad (5)$$

In order to generate this first-order model, the second-order structural modal model must be converted to a first-order model and the linear optical mode] must be prepended to the resultant measurement equation. The second order modal model form is given in Eq.6.

$$\ddot{\vec{\eta}} + 2Z\Omega\dot{\vec{\eta}} + \Omega^2\vec{\eta} = \Phi^T B_f \vec{f} \quad \text{(state equation)}$$
$$\vec{d} = \Phi\vec{\eta} \quad \text{(measurement equation)} \quad \mathbf{(6)}$$

In order to keep tbc dynamic analysis simple, the damping matrix is generally assumed to be diagonal with small damping values. Modal damping values arc assigned somewhat arbitrarily based on inherent material damping characteristics and expected damping dttc to dissipative forces in joints, cables, etc. A uniform modal damping of 1% was assumed for all flexible-body modes included in the integrated mode].

$$\gamma_i = \frac{\sqrt{(b_{mi}^T b_{mi})(c_{mi}^T c_{mi})}}{4\zeta_i \omega_i^2} \quad (7)$$

where, **γi** is the Hankel singular value for mode i
$b_{m,i}$ is the i'th column of B_m
c_{mi} is the i'[h column of C_m
i is the nodal index
where,

$$B_m = \Phi^T B_f \quad (7a)$$

and,

$$C_m = C_{opt}\Phi \quad \mathbf{(7b)}$$

In order to reduce disturbance analysis complexity and computational time, only a subset of the flexible-body modes is included in the end-to-end disturbance model, The modes chosen to be included arc all of the rigid-body modes and the flexible-body modes that have the highest Hankel Singular Values (known as "second-order modes" of the internall y balanced rcali~.alien in [10]). Hankel singular values arc a measure of the controllability and observability of a mode. Hankel singular values, for small modal damping values, arc approximated by Eq.7.

If the input arc disturbances and the output arc performance metrics, then the Hankel singular values arc a measure of the significance of the mode to the disturbance analysis. The Hankel singular values for the flexible-body

modes below 1000Hz arc plotted in Fig. 13. The fifteen most significant flexible-body modes were chosen to be included in the end-to-end disturbance model,

The second order modal model is converted to a firs~-order model by lhc use of the following substitution:

$$\vec{x} = \begin{bmatrix} \vec{\eta} \\ \dot{\vec{\eta}} \end{bmatrix} \qquad (8)$$

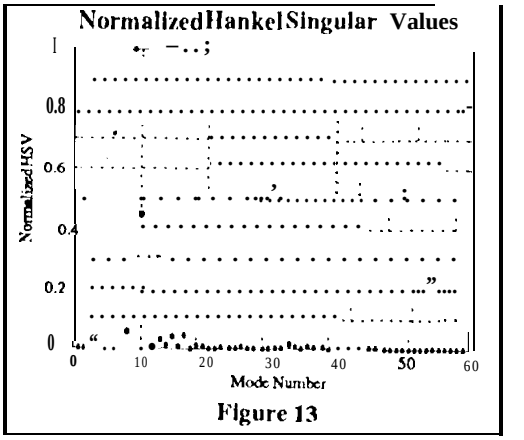

Figure 13

This modal model to state space conversion capability is available in 1 MOS. The result of this conversion is a first-order state-space mode] whose input arc the desired disturbance force input, and whose output arc nodal displacements. Since the linear optical C-matrix maps a nodal displacem ent vector to the desired optical output (OPD variations), by prc-multiplying the system C-matrix and D-matrix resulting from the above substitution by the optical C-matrix, the. output of the linear model becomes the desired top and bottom starlight interferometer OI 'D variations.

7.2 Frequency Response Function (frf) Analysis

After the first-order end-to-end model is generated, frequency response transfer functions arc calculated using standard Pro-Matlab functions. These transfer functions relate the magnitude of the output of tbc linear system to the magnitude of the input as a function of frequency [11]. For a linear system, a transfer function is a property of the. system itself and dots not depend on the input. l'bus, examination of frequency response functions (frfs) yields insight into the qualities of a system.

Frequency response functions arc generated from the fifteen reaction wheel disturbance input (five disturbances pcr wheel, three wheels) to the two starlight OPD variations. This results in a total of thirty transfer functions. The six frequency response functions for reaction wheel radial disturbances for all wheels to the upper starlight interferometer OPD variation arc displayed in Fig. 14. These frfs arc typical of the disturbance input to OPD variation output frfs. The peaks in the frf correspond to ftcxiblc-body modes. The height of the peak depends on the modal damping, the excitability of the mode, and the sensitivity of the OPD variations to the modeshape. These factors arc all accounted for in the calculation of the Hankel singular values [10]. The flexible-body modes arc superimposed on the familiar -40dB/decade slope that corresponds to the force-to-displacement transfer function of a rigid-body mode [1 1].

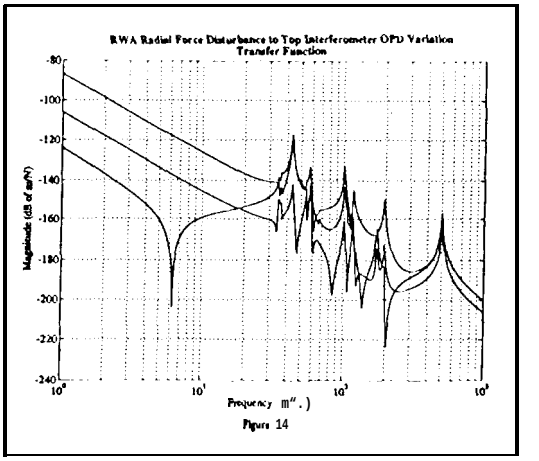

Figure 14

8. End-to-End Reaction Wheel Di turbance Analysis

Using the firs[-order end-to-end system mode], the OPD variation duc to reaction wheel disturbances can bc found by multiplying the disturbance component amplitudes by the transfer function magnitude at the disturbance component frequencies. This gives a corresponding OPD variation at the disturbance component frequencies. The rms OPD variation is then found from Eq.4, and the resulting fringe coherence is calculated according to Eq.5. This reaction wheel induced fringe coherence will vary as the wheel speed varies. Since the reaction wheel bias speed will vary in some random fashion as the reaction wheels counter external torques, fringe coherence is assessed at all wheel speeds (O to 3000 r-pm) for each of the three wheels, The result is six graphs of fringe coherence versus reaction wheel speed (one graph for each combination of three RWAS and two fringe coherences). A sample of these results (fringe cohcrcncc as a function of the speed of the, reaction wheel along the x-axis) is shown in Fig. 15. The corresponding rms OPD variations arc shown in Fig. 16. The fringe coherences were dctcrrnincd for an optical wavelength of 0.25µm and a detector integration time of 0.2s.

The dips in the fringe coherences depicted in Fig. 16 occur when a reaction wheel disturbance component excites a particularly offensive structural mode, causing a large OPD variation. Since the reaction wheel disturbance

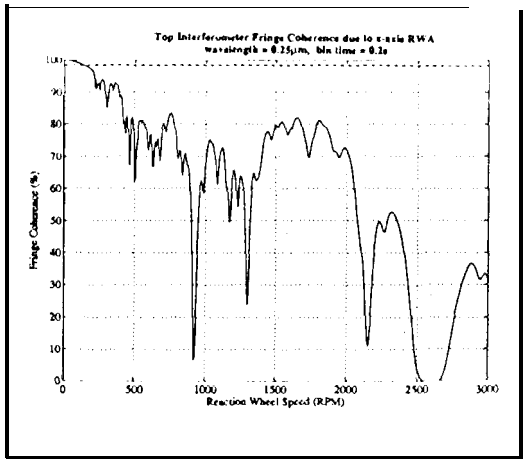

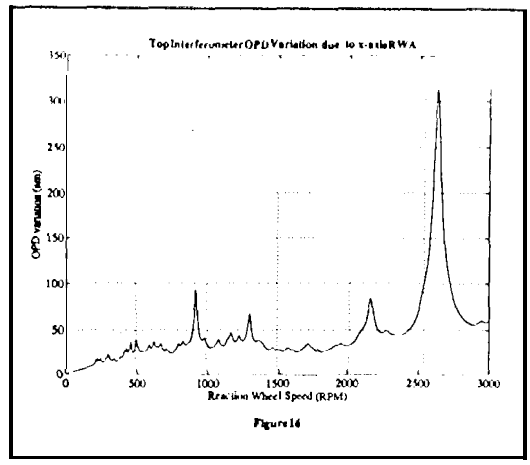

Figure 16

spectra arc fairly rich in frequency content (i.e., there arc many frequency components), this occurs for a large portion of reaction wheel speeds.

The total fringe coherence rcquircmcnt is 95%. This rcquircmcnt should be applied to the fringe coherence that results from the disturbances of all three wheels. This total fringe coherence is simply the product of the separate coherences, since the disturbances duc to onc reaction wheel arc statistically independent of the disturbances of the other wheels. Therefore the fringe cohcrcncc requirement for each of the three wheels is the cube root of the total fringe coherence requirement, 98.3%. The dashed line in the graph rcprcscnts this separate fringe cohcrcncc requirement.

It is clear that the total fringe coherence for both the top and bottom interferometers is below the requirement of 95% for a large combination of the three wheel speeds, and for several wheel speeds, the coherence is seriously degraded (→ O). Correspondingly, the OPD variations arc as much as 1.5 orders of magnitude larger than the requirement (12.7 nm).

9. Evaluation of Design Improvement Options

End-to-end reaction wheel disturbance analyses were used to evaluate. the effectiveness of both reaction wheel disturbance isolation and structural damping.

9.1 Structural Damping

Structural damping refers to the placement of passive and/or active damping struts in the interferometer truss structure, hence increasing the damping of the structural modes. Optimal damping placement is performed by targeting either a certain set of troublesome modes or a particular frequency band. The desired number of passive/active damping struts arc chosen, and a large optimization problem is solved to determine the optimal damper placement and parameters [12]. This process requires a very accurate structural finite element model, along with the ability to model discrete damping elements (as opposed to distributed or modal damping).

Since the detailed FEM is unavailable, it "is inappropriate to perform a damper placement optimization.

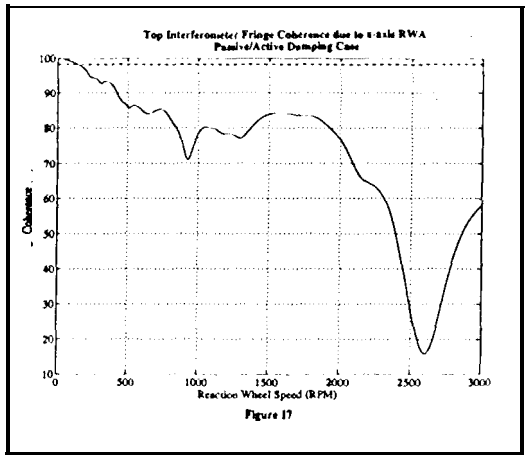

Figure 17

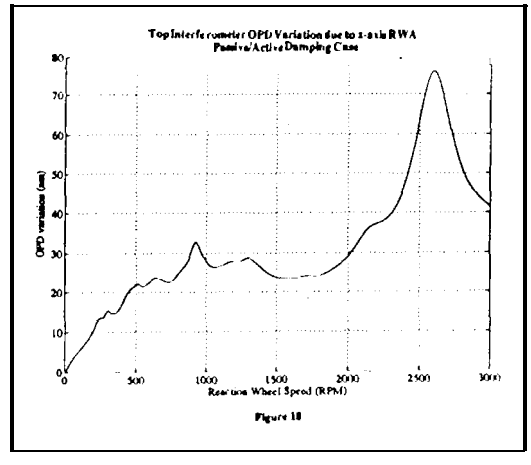

Figure 18

Results characteristic of this placement process arc modeled by assigning higher modal damping to the targeted modes in the finite element model. The assigned damping is determined from typical damper placement results, such as those attained for the Controls Structures Interaction (CSI) Phase B testbed 113]. In the case of the Phase B testbed, modal damping of 5% was attained for the, significant modes.

It is important to note that these results arc model dependent, and therefore that this analysis is a rough estimate. Even so, this assumption is the first step towards encompassing the capabilities of active/passive structural damping using discrete damping struts. A modal damping of 5% for all modes was used to assess the effectiveness of damping strut technology. A sample of the results of the end-to-end analysis arc shown in Fig.17 and Fig.18. Although the addition of ~assivc/active damping caused an improvement in the sensitivity of the coherence to reaction wheel vibrations, 'the fringe coherence requirement was not met for a large range of wheel speeds.

9.2 Disturbance Isolation

Disturbance isolation entails placing the reaction wheels on a six-dof, isolated platform, The isolation system would consist of passive damping struts similar to those used to isolate the }1S'1' reaction wheels [14]. These passive isolators act as a mechanical lowpass filter for the reaction wheel disturbances. The two pertinent parameters for the isolation system arc the isolator break frequency and the damping.

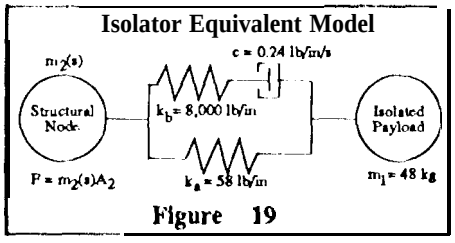

Figure 19

The isolators arc modeled as a two-spring, single-das}lpot system (shown in Fig.19) [15]. Although the stiffnesses and damping arc tunable over a large range, typical parameters were used in the isolator model (see Fig. 19)[1 5]. The force. input to force output transfer function of the isolator, given in Eq.9, is essentially a second order system. The analysis assumed that there is no dynamic interaction between the isolator and the structure ($m_2(s) >> m_1$ Vs, $m_p \approx m_1$). Although in general this is not true, the assumption is justified by the simplification of tbc analysis. Also, since the isolator break frequency (4 Hz) is much lower than the lowest structural mode (34.611x), the dynamic interaction should be minimal.

$$\frac{F_{out}}{F_{inp}} = \frac{m_p}{m_1 m_p c s^3 + m_p k_b s^2 + (k_a + k_b) c s + k_a k_b} \left[(k_a + k_b) c s + k_a k_b \right] \quad (9)$$

Where m_p is the parallel mass:

$$m_p = \frac{m_2(s) m_1}{m_2(s) + m_1} \quad (9a)$$

where $m_2(s)$ is the force to acceleration transfer function at the attachment point of the isolator.

The isolators were modeled by filtering the input disturbances with the isolator transfer function (Eq.9). These filtered disturbances were then used as input to the end-to-end model as described above. The fringe coherence for the isolated disturbances is given in Fig.20, and the OPD variations arc given in Fig.21. The addition of the isolators yielded an overall improvement of the sensitivity of fringe coherence to reaction wheel vibration across the band of RWA speeds. The isolator resonance itself, however, caused the total coherence to degrade below 95% for

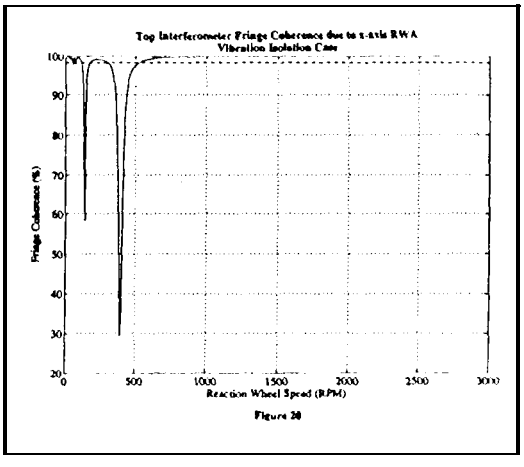

Figure 20

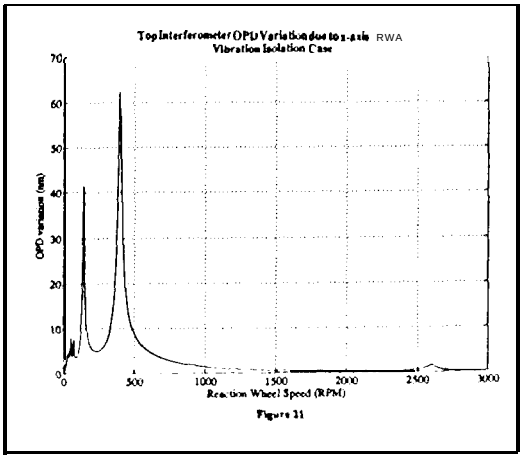

Figure 21

wheel speeds below 500rpm. It appears that the fringe coherence requirement could be met if wheel speeds were kept above 500rpm, or if the damping of the isolation system could be increased.

10. Conclusions

The prelim inary POINTS spacecraft design was presented and the sensitivity of the starlight interferometers to structural motion and attitude jitter as they affect total starlight OPD was established. OPD variations during a star pair observation degrade the ability of the instrument Kalman filters to track fringes. This led to the establishment of fringe coherence as a performance metric. This fringe coherence accounts for both OPD variations and instrument filter integration time. It was assumed that the fringe coherence during the detector integration time (<0.2s) must be greater than 95% in order for the fringe tracking filters to operate,

An end-to-end disturbance analysis was performed in order to assess the fringe coherence of the preliminary POINTS design. This end-to-end analysis included a structural finite element model, a linear optical model, and a mechanical disturbance mode.1. Reaction wheel mechanical disturbances were the only expected mechanical disturbances. Reaction wheel radial force, axial force, and radial torque disturbances were modeled for three wheels. These disturbances are all a function of the reaction wheel speeds. The result of the end-to-end disturbance analysis is a plot of fringe coherence as a function of reaction wheel speed for each wheel. The fringe coherence for both the top and bottom interferometers was found to be well below the requirement of 95% for virtually all wheel speeds.

The end-to-end disturbance model was then used to assess the effectiveness of two possible solutions to the. mechanical disturbance problem: 1) use of passive or active damping struts to increase modal damping, and 2) use of a passive reaction wheel vibration isolation system to reduce disturbance input to the structure. In order to" assess the effectiveness of passive/active damping struts, higher modal damping values were assumed commensurate, with results obtained from actual testbed damper placement results. The addition of passive/active damping struts resulted in a significant improvement in fringe coherence, however the fringe coherence requirement was still not met for a large range of wheel speeds. For the vibration isolation solution, an existing isolation system design with a break frequency of 4Hz was used to filter the input disturbances. The vibration isolation system yielded reduced OPD variations markedl y for wheel speeds above 500rpm. The isolator resonance itself, however, caused the coherence to degrade far below 95% for wheel speeds below 500rpm.

The isolator and passive/active damping solutions modeled in these analyses are not optimum solutions. In the case of damper placement, it may be more advantageous to target specific structural modes, and the improvement in structural damping may be more or less than that assumed in the analysis. Similarly, it is clearly beneficial, in terms of disturbance isolation, to have as much isolator damping as possible, It is not yet understood how much damping is available from these passive vibration isolation systems. The initial results show that the structure with a vibration isolation system can meet the fringe coherence requirement, if either the reaction. wheel speeds are kept above 500rpm, or if the isolation system damping is higher.

11. Acknowledgments

This work was performed at the Jet Propulsion Laboratory, California Institute of Technology, under contract with the National Aeronautics and Space Administration. The authors would like to thank R. D. Reasenberg, B.L. Schumaker, and J. D. Phillips for their patience and perseverance in explaining the operation of the POINTS instrument and instrument filter; C. Satter for her aid in formulating a finite element model of the POINTS strut.turw D. C. Redding for his responsiveness to the special optical modeling needs required for POINTS modeling effort; and finally and most importantly, R. A. Laskin and B.L. Schumaker for the guidance and commitment of resources that made this work possible.

12. References

1. J. Melody, "POINTS Pointing System Requirements and Possible Architectures, " JPL IOM 343-92-542, October 1992.
2. D. Eldred, J. Melody, "POINTS Gimbal Configuration Preliminary Design, " JPL IOM 3.43-91-576, August 1991.
3. C. Satter, "Summary of POINTS Structural Design, Modeling, & Analysis FY'92 to date," JPL IOM 3542/CS/543-92, December 1992.
4. R. D. Reasenberg, POINTS Technical Presentation to the Space Interferometry Science Working Group (SISWG), SAO, February 1992.
5. S. W. Sirlin, A. M. San Marlin, "A New Definition of Pointing Stability, " JPL EM 343-1189, March 1990.
6. The Math Works, Inc., "Matlab User's Guide, For UNIX Workstations," August 1992.
7. }1. C. Briggs, "Integrated Modeling of Optical Systems User Guide, Release 1.0," JPL D-9836, June 1992.

8. D. C. Redding, "Controlled Optics Modelling Package User Manual, Release 1.0," JPL IOM, 1).9816, June 1992.
9. M.D. Hasha, "Reaction Wheel Mechanical Noise Variations," LMSC EM SSS 218, June 1986.
10. C. Z. Gregory, Jr., "Reduction of Large Flexible Spacecraft Models Using Internal Balancing *Theory," Journal of Guidance and Control,* Vol.7, *Nov.* -Dec. *1984,* pp.725-732.
11. B. C. Kuo, *Automatic Control Systems,* Prentice-Hall, Inc., Fifth Edition, 1987.
12. C. C. Chu, M. Milman, "Paper on the Usc of Ritz Model Reduction Techniques in the Modeling and Analysis of Viscous Dampers in Structures," JPL IOM, August 1991.
13. J. Spanos, Z. Rahman, C. Chu, J. O'Brien, "Control Structure Interaction in Long Baseline Space Interferometers," 12th IFAC Symposium on Automatic Control in Aerospace, Ottobrunn, Germany, September 1992.
14. J. J. Rodden, H. J. Dougherty, L. P. Reschke, M. D. Hasha, "Line of Sight Performance Improvement with Reaction Wheel Isolation, " AAS 86-005, Annual AAS Guidance and Control Conference, Keystone, CO, February 1986.
15. D. Cunningham, P. Davis, F. Schmitt, "A Multiaxis Isolation System for the French Earth Observation Satellite's Magnetic Bearing Reaction Wheel, " Proceedings of the ADPA/AIAA/ASME/SPIE Con ference on Active Materials and Adaptive Structures, Alexandria, VA, November 1991.